

Numerical Modeling of Runback Water on Ice Protected Aircraft Surfaces

Kamel M. Al-Khalil*

National Research Council, Washington, D.C. 20418

and,

Theo G. Keith, Jr.†, Kenneth J. De Witt‡

The University of Toledo, Toledo, Ohio 43606

S11-34-
160471
P. 12

A numerical simulation for "running wet" aircraft anti-icing systems is developed. The model includes breakup of the water film, which exists in regions of direct impingement, into individual rivulets. The wetness factor distribution resulting from the film breakup and the rivulet configuration on the surface are predicted in the numerical solution procedure. The solid wall is modeled as a multi-layer structure and the anti-icing system used is of the thermal type utilizing hot air and/or electrical heating elements embedded within the layers. Details of the calculation procedure and the methods used are presented.

Nomenclature

<p>C_p = specific heat</p> <p>F = wetness factor</p> <p>h_i = heat transfer coefficient between the hot air and the inner surface of the wall</p> <p>h_w = heat transfer coefficient between the outer surface of the wall and the runback water</p> <p>h_∞ = heat transfer coefficient between the free stream and the outer surface of the wall</p> <p>k = thermal conductivity</p> <p>L_v = latent heat of vaporization of water</p> <p>LWC = liquid Water Content</p> <p>M = molecular mass, number of grids across film</p> <p>m = runback water mass flow rate</p> <p>m'' = rate of mass transfer per unit area</p> <p>P = static pressure</p> <p>Pr = Prandtl number</p> <p>q = rate of heat transfer</p> <p>q'' = rate of heat transfer per unit area</p> <p>\dot{q} = rate of heat generation per unit volume</p> <p>R = rivulet radius</p> <p>r = recovery factor</p> <p>Sc = Schmidt number</p> <p>V = flowfield velocity</p>	<p>w = velocity in a rivulet in the flow direction</p> <p>T = temperature</p> <p>α = thermal diffusivity</p> <p>β = rivulet contact angle with the solid surface</p> <p>δ_f = equivalent rectangular film thickness of a rivulet</p> <p>λ = ratio of rivulet width to wetness factor, or distance between two adjacent surface streamlines</p> <p>η = droplet collection efficiency</p> <p>μ = dynamic viscosity of water</p> <p>ξ = area correction factor for heat loss from a rectangular film to the ambient</p> <p>ρ = density</p> <p>τ = surface shear force (friction)</p> <p>ϕ_∞ = free stream relative humidity</p> <p><u>Subscripts</u></p> <p>a = anti-ice air</p> <p>a_i = anti-ice</p> <p>e = property at edge of the boundary layer</p> <p>$evap$ = evaporation from outer cowl surface</p> <p>f = liquid film</p> <p>imp = impingement on outer cowl surface</p> <p>m = solid wall composed of several layers</p> <p>r = rivulet</p> <p>vap, v = vapor, saturated vapor</p> <p>w = wall or runback water</p> <p>∞ = at free stream conditions</p>
---	---

* NRC Research Associate, *NASA Lewis Research Center*.

† Professor, *Mechanical Engineering Dept.*

‡ Professor, *Chemical Engineering Dept.*

Superscripts

- l = layer number in the composite wall
 n = Δz step level (grid number in the z-direction)

I. Introduction

The problem of aircraft icing has been the focus of study of many researchers for a number years. The detrimental effects of ice accretion on critical surfaces can jeopardize flight safety as well as the overall aircraft performance. Consequently, accurate modeling and extensive study of the icing process are necessary. Two general methods of ice protection have been developed: De-icing methods for the intermittent removal of ice buildup by destroying the bond between the ice and the surface, and anti-icing methods for the prevention of ice formation on critical surfaces such as engine nacelles.

The availability of high-speed digital computers has favored the use of numerical techniques and the development of computer codes to design and analyze ice protection systems. It is felt that the latter can minimize the cost associated with the required experimental testing by providing a tool that is at least capable of predicting preliminary results.

Most studies related to aircraft icing have been committed to the prediction of ice shapes and the determination of their detrimental effects on aerodynamic performance of the aircraft components. At this time, research in running wet anti-icing systems is quite basic, and runback is treated in a primitive manner. The NASA Lewis Research Center has been a major contributor in conducting and sponsoring studies related to computer modeling of aircraft icing processes as well as experimental testing in its Icing Research Tunnel (IRT). As a result, LEWICE [1], an ice accretion prediction code, was developed for unprotected airfoil surfaces. The approach used in the modeling consists of performing mass and energy balances on the surface water. The wetness factor issue is ignored and the runback water is assumed to wet the entire surface at a particular location. Consequently, the amount of required heat to anti-ice the surface is under-estimated.

Several investigators have produced different versions of the LEWICE code in order to improve it. To name a few, Cebeci et. al [2] modified the flowfield calculation module of the code to avoid the problem of multiple stagnation points. Yamaguchi et. al [3] proposed a multi-zone roughness model: a zone of uniform water film in the stagnation region, a rough zone of stationary water beads, and lastly, a zone where surface water run back as rivulets [4]. The runback water was recently modeled by Al-Khalil et. al [5,6,7] by incorporating a rivulet model. This paper is intended to present the numerical calculation procedures used including the most recent improvements of the latter model.

II. Mathematical Model

The runback model introduced earlier is based on a two-dimensional mathematical formulation. The surface water and the solid structure temperatures vary across their

thicknesses and in the flow direction along a streamline on the surface. Spanwise temperature dependence is assumed to be negligible. However, the latter is accounted for by performing energy balances on control volumes whose spanwise widths extend between two adjacent streamlines on the aircraft surface.

II.1 Runback Water

II.1.1 Hydrodynamics:

The rate of water impingement on aircraft surfaces, due to the existence of undisturbed supercooled liquid water droplets in clouds, is relatively small. This and aerodynamic forces result in a very shallow water film flowing over the skin surface. Consequently, the surface water behavior is controlled not only by aerodynamic and body forces, but also by surface tension forces and surface roughness.

In the direct impingement regions, i.e., in the neighborhood of the stagnation point, the water tends to wet the entire surface due to incoming droplets and due to water running back from upstream locations. However, at or downstream of the impingement limit, the liquid film could become unstable due to surface tension forces that cause the surface water to coalesce into individual streams, referred to as rivulets, separated by dry areas.

A detailed study on the hydrodynamics and a stability analysis of surface water was presented in Ref. [5]. For completeness, some of the essential features are presented here without further discussion. The film/rivulet flow in the streamwise (z) direction is caused by a shear force acting at the liquid-air interface. The latter force is obtained from the results of the skin friction factor computed from viscous aerodynamic calculations of the flowfield.

A rectangular film model was chosen to mathematically represent the heat transfer process in a rivulet as shown in Fig 1. This model was found appropriate to the current problem for various reasons discussed in Ref. [6]. The criteria used for the new runback water configuration are as follows:

- The wetness factor is preserved, i.e., the widths of a rectangular film is equal to that of its corresponding rivulet.
- The law of mass conservation requires equal mass flow rates in a rivulet and its equivalent rectangular film. This criterion enables one to compute the film thickness δ_f .
- Mass loss due to evaporation is associated with a decrease in the rivulet size, i.e., its radius and, consequently, its base width that is also equal to the rectangular film width. This criterion enables one to update the value of the wetness factor.

The velocity distributions within the film and the rivulet were derived and used to obtain the mass flow rates in each [5], as shown, respectively:

$$m_f = \frac{\rho \lambda F \tau}{2 \mu} \delta_f^2 \quad (1)$$

$$m_r = \frac{\rho \tau F_1(\beta)}{\mu} R^3 \quad (2)$$

The second criterion is used, equating the above equations, to give:

$$\delta_f = R \sqrt{\frac{F_1(\beta)}{\sin\beta}} \quad (3)$$

where $F_1(\beta)$ is a function of β derived in [7]. The above equation shows the rectangular film thickness is directly proportional to its equivalent rivulet radius. This equation will later be used to update δ_f when R is reduced due to evaporation. Procedures to determine the conditions and location for the breakup of the liquid layer flowing downstream of impingement regions were thoroughly discussed in Ref. [5]. The prediction of initial values of R and F at breakup was also described.

II.1.2 Thermal Analysis:

The principal objective of this study has been to analyze and predict the performance of anti-icing systems. In such applications, the worse case occurs at equilibrium state conditions. Consequently, the mathematical formulation of the heat transfer process is based on the steady-state energy equations. The unsteady equations are more relevant to de-icing applications. The runback water energy equation then follows:

$$\frac{\partial T_w}{\partial z} = \gamma \frac{\partial^2 T_w}{\partial y^2} \quad (4)$$

$$\text{where, } \gamma = \frac{\alpha_w}{w(y)}$$

The above equation is based on the fact that conduction heat transfer within the liquid water in the z -direction (flow direction) is negligible compared to that in the y -direction (across film thickness). The solution of Eq. (4) requires two boundary conditions in the y -direction, one at the solid-liquid interface, and one at the liquid-air interface, and an initial condition ($z=0$). The latter condition requires knowledge of the water temperature at the stagnation point. Analytically, this is impossible because that depends on the final temperature solution in the water film and in the solid structure layers. However, this may be obtained numerically in an iterative procedure described in a later section.

The boundary condition at the liquid-air interface is written as:

$$-k_w \frac{\partial T_w}{\partial y} = h_\infty \xi \left[T_w - T_e - \frac{r V_e^2}{2 C_{p,air}} \right] + m_{evap} \xi L_v - m_{imp} C_{p,w,\infty} (T_\infty - T_w) - \frac{m_{imp} V_\infty^2}{2} \quad (5)$$

where the first and second term terms on the right-hand side represent heat loss to the ambient by convection and evaporation, respectively; and the third and fourth terms are the sensible and kinetic heat contributions of the

impinging droplets which are of value only in the direct impingement region.

The rate of impingement per unit area, m''_{imp} , is calculated from the local value of the collection efficiency as shown:

$$m''_{imp} = \eta LWC V_\infty \quad (6)$$

and the rate of evaporation per unit area is computed using the Chilton-Colburn heat-mass transfer analogy. This may be expressed as:

$$m''_{evap} = \frac{h_\infty}{C_{p,air}} \left(\frac{Pr}{Sc} \right)_{air}^{2/3} \frac{M_{H_2O}}{M_{air}} \left[\frac{P_{v,w} - P_{vap}}{P_e - P_{v,w}} \right] \quad (7)$$

where,

$P_{v,w}$ = saturated vapor pressure at the local runback water temperature T_w .

P_{vap} = local vapor pressure at the edge of the boundary layer at the local relative humidity.

Application of Dalton's Law of partial pressures and knowledge of ambient conditions yields:

$$P_{vap} = P_e \frac{P_{v,\infty}}{P_\infty} \phi_\infty \quad (8)$$

where the relative humidity ϕ_∞ in a cloud is generally taken to be 100%. The saturation vapor pressure of water is written as function of temperature:

$$P_v(T) = 2337 \exp \left\{ 6789 \left[\frac{1}{293.15} - \frac{1}{T} \right] - 5.031 \ln \left[\frac{T}{293.15} \right] \right\} \quad (9)$$

where the units of P_v and T are (Pa) and (K), respectively.

The recovery factor r in Eq. (5) accounts for viscous dissipation in the boundary layer and is approximated by [8]:

$$r = 1 - \frac{V_e^2}{V_\infty^2} (1 - Pr_{air}^n), \quad n = \begin{cases} \frac{1}{2} & \text{laminar flow} \\ \frac{1}{3} & \text{turbulent flow} \end{cases} \quad (10)$$

The properties at the edge of the boundary layer, i.e., P_e , T_e , and V_e are computed using the perfect gas relations for isentropic flow and the local values of the pressure coefficient obtained from a flowfield solver.

Note that ξ , in Eq. (5), is an area correction factor to account for the area differences in the rivulet and the rectangular film models through which heat exchange with the ambient occurs. This factor is defined as the ratio of the rivulet free surface area to the upper surface area of the corresponding rectangular film. From geometric considerations, the following may be written:

$$\xi = \frac{\beta}{\sin\beta} \quad (0 < F < 1) \quad \left. \vphantom{\xi} \right\} \quad (11)$$

$$\xi = 1 \quad (F = 1) \quad \left. \vphantom{\xi} \right\}$$

This factor is less than 10% for contact angles smaller than 42°, and is unity for uniform film flow.

The boundary conditions concerning the solid-liquid interface which represents the heat exchange between the solid wall and the runback water remains to be discussed. These two conditions will be presented with the energy equation of the wall structure since they are common between the two regions.

II.2 Anti-Ice Bleed Air:

A widely used method of preventing ice formation is the hot air type due to its high reliability. In these systems, hot air is drawn from an intermediate or high stage compressor bleed port and ducted through passages to the leading edges of wings, empennages, engine nacelles or other critical areas. Due to the complexity of the flow of the anti-icing air inside the irregular duct shapes and the uniqueness of each design, a generalized model requires the following assumptions:

1. The heating requirement by such a system is generally specified by the amount of hot air supply, m_a , and its delivery temperature at the stagnation region.
2. The internal heat transfer coefficients h_i , between the air and the inside surface of the structure, is assumed to be known from previous experience or from experimental testing on the particular system in consideration.
3. The hot air temperature varies in the flow direction and is assumed to be lumped in the transverse direction.

With regards to the above assumptions, the energy equation of the anti-ice air may be written as:

$$m_a C_{pa} \frac{dT_a}{dz} = h_i(z) [T_a(z) - T_m(y=0, z)] \quad (12)$$

Obviously, $T_a(z)$ depends on the solid wall temperature distribution which also depends on the runback water solutions. Therefore, the energy equations of those three regions must be solved simultaneously.

II.3 Wall Structure:

Based on the assumption that the wall temperature is dependent on the y and z -direction [6], the following energy equation may be written for each layer in the composite structure:

$$\frac{1}{\lambda(z)} \frac{\partial}{\partial z} \left[\lambda(z) \frac{\partial T_m}{\partial z} \right] + \frac{\partial^2 T_m}{\partial y^2} + \frac{q^0}{k_m} = 0 \quad (13)$$

where $\lambda(z)$ may be taken as the distance between two adjacent surface streamlines which make up the strip being analyzed. This distance is constant for a 2-dimensional flow over a surface. The above formulation allows one to model a heating element as one of the layers. If anti-icing is achieved by means of a hot air system alone, the value of q^0 may be conveniently set to zero for all the layers.

The boundary condition at the inner surface of the wall may be written for the innermost layer as:

$$-k_m \frac{\partial T_m}{\partial y} = q_{ai}^0 + h_i (T_a - T_m) \quad (14)$$

where q_{ai}^0 is an optional prescribed heat flux distribution. This value and h_i may be set to zero for a perfectly insulated inner surface. The above equations were formulated as such to give the flexibility of modeling different systems.

The two conditions that must be satisfied at each solid-solid interface between the wall layers are continuity of temperature and heat flux normal to the interface. As to the boundary conditions on the left side (stagnation point) and the right side of the wall, they may be extrapolated from the solutions using insulated conditions, or they may be specified if the temperature distribution is known at either end.

The last boundary conditions that remain are those pertaining to the outermost layer at the solid-liquid (partially or fully wetted surface) and solid-air (dry surface) interfaces. They may be written as follows:

$$T_m = T_w \quad (0 \leq F < 1) \quad (15)$$

and,

$$q_m^0 = -k_w F \frac{\partial T_w}{\partial y} + h_w (1-F) (T_m - T_e - \frac{r V_e^2}{2 C_{pair}}) \quad (0 \leq F \leq 1) \quad (16)$$

The first condition is only necessary in the fully or partially wetted regions. The second condition simply states that heat, q_m^0 , is transferred from the wall proportionally through the wetted (to the water) and the dry (to the ambient) surface areas as defined by the wetness factor F . Note that T_m , in Eq. (16), may be replaced with T_w according to Eq. (15).

III. Numerical Solution Techniques

III.1 Runback Water:

A fully implicit method was used to numerically solve Eq. (5) because of the positive stability properties [9]. Backwards differencing in the z -direction, and central differencing in the y -direction were employed. Applying this scheme to Eq. (5) and rearranging terms yields:

$$-\left[\frac{\gamma_j \Delta z}{2 \Delta y^2} \right] T_{j-1}^{n+1} + \left[1 + \frac{\gamma_j \Delta z}{\Delta y^2} \right] T_j^{n+1} - \left[\frac{\gamma_j \Delta z}{2 \Delta y^2} \right] T_{j+1}^{n+1} = T_j^n \quad (17)$$

for $j=2, 3, \dots, M-1$, where M is the total number of grid points across the film thickness (in the y -direction), and n is the grid number in the flow direction (z). Equation (17) is written for each corresponding node which results in a set of linear equations. The latter may be rewritten in a matrix form and solved using the Thomas Algorithm for tridiagonal system of equations.

However, before carrying the solution, two equations, corresponding to $j=1$ (solid-liquid boundary) and $j=M$ (liquid-air boundary), are still required. A one-sided difference representation of Eqs. (16) and (5) is used for

this purpose, respectively. Equation (15) could have been used in the runback solution while Eq. (16) is used in the wall solution, instead. However, that procedure was found to be highly unstable. Thus:

$$\left[1 + \frac{h_{\infty} (1-F) \Delta y}{F k_w} \right] T_j^{n+1} - T_{j+1}^{n+1} = \frac{\Delta y}{F k_w} \left[q_m'' + h_{\infty} (1-F) \left(T_e - \frac{r V_e^2}{2 C_{pair}} \right) \right] \quad (18)$$

where $j=1$, and q_m'' is the rate of heat flux normal to the solid-liquid interface computed from the temperature distribution in the wall from the following:

$$q_m'' = -k_m \frac{\partial T_m}{\partial y} \quad (\text{at solid-liquid interface}) \quad (19)$$

A second order finite differencing was used to compute the right-hand side of Eq. (19). At $j=M$, one may write, after rearranging terms:

$$-T_{j-1}^{n+1} + \left[1 + \frac{\Delta y}{k_w} (h_{\infty} \xi + m_{imp}'' C_{p_{w,m}}) \right] T_j^{n+1} = \frac{\Delta y}{k_w} \left[h_{\infty} \xi \left(T_e + \frac{r V_e^2}{2 C_{pair}} \right) - m_{evap}'' L_v \xi + m_{imp}'' \left(C_{p_{w,m}} T_m + \frac{V_m^2}{2} \right) \right] \quad (20)$$

The above equations may now be solved for the temperatures at nodes $j=1$ through M at location $z+\Delta z$ (i.e., $n+1$), knowing the nodal temperatures at location z (i.e., n). The evaporation term m_{evap}'' is computed using the temperature at z in order to preserve the linearity of the system of equations.

The procedure described above requires knowledge of the water temperature at the stagnation point ($z=0$, or $n=1$). This is obtained by extrapolation from the temperature distributions at $n=2$ and $n=3$. Since the solution procedure is iterative, as discussed later, an initial guess is required to start the computations. This is achieved by performing mass and energy balances on a differential control volume of the surface water at the stagnation point, which yields the following approximate expression:

$$T_w^{n+1} (\text{initial}) = \left[m_{imp}'' \left(C_{p_{w,m}} T_{\infty} + \frac{V_m^2}{2} \right) - m_{evap}'' L_v + q_m'' + h_{\infty} \left(T_e + \frac{r V_e^2}{2 C_{pair}} \right) \right] / (m_{imp}'' C_{p_{w,m}} + h_{\infty}) \quad (21)$$

where q_m'' is estimated assuming that heat conduction within the solid structure occurs in the outward direction (y). Equation (21) is only used at the first iteration. In subsequent iterations, the extrapolation technique mentioned previously may be used. However, this caused slight fluctuations in the temperature distribution at the first few nodes ($n=1,2,3,4$). The problem was remedied by setting the initial water temperature equal to the average temperatures of nodes $n=2$ and 3 without affecting the remaining results.

In addition to an initial temperature, an initial water film thickness is required. A mass balance may be

performed on a control volume of length Δz_1 (distance between node $n=1$ and $n=2$), thickness δ_f , and a unit depth. Using Eq. (1) with $\lambda=1$ and $F=1$, this yields:

$$(m_{imp}'' - m_{evap}'') \Delta z_1 = \frac{\rho \tau}{2 \mu} \delta_f^2$$

Solving for δ_f , gives:

$$\delta_f^{n+1} (\text{initial}) = \sqrt{\frac{2 \mu \Delta z_1}{\rho \tau} (m_{imp}'' - m_{evap}'')} \quad (22)$$

where τ is taken as the average wall shear force between nodes $n=1$ and $n=2$.

The conservation of mass equation of the runback water may be readily obtained and shown to be:

$$m^{n+1} = m^n + \lambda^{n+1} \Delta z (m_{imp}'' - m_{evap}'' \xi) \quad (23)$$

Knowing the mass flow rate, the film thickness in the fully or partially wetted regions may be derived from Eqs. (1), (2) and (3):

$$\delta_f^{n+1} = \sqrt{\frac{2 \mu m^{n+1}}{\rho \tau \lambda}} \quad (F=1) \quad (24)$$

$$\delta_f^{n+1} = \left[\frac{m_r^{n+1} \mu}{\rho \tau F_1(\beta)} \right]^{1/3} \sqrt{\frac{F_1(\beta)}{\sin(\beta)}} \quad (0 < F < 1) \quad (25)$$

where m_r is the mass flow rate per rivulet. In the case where the runback water is flowing as rivulets ($F < 1$), the wetness factor must be updated at each z -location. From geometric considerations, this is derived from $F = (2R \sin \beta) / \lambda$ where R is obtained from Eq. (3). However, if surface streamlines are not parallel (3-D flow), great care must be taken when evaluating λ to account for variations in the distance between two surface streamlines which identify the strip being analyzed.

The numerical solution of Eqs. (17), (18) and (20) requires the discretization of the water domain into grid points. Across the liquid layer thickness, equal spacing between the grid points was used. Along the flow direction, two zones were selected: direct impingement region, and downstream region. The grid spacing is constant in each zone, but is much smaller in the direct impingement region to accommodate for the rapidly changing variables due to the impinging water droplets and the flowfield characteristics.

The current model was specifically developed for anti-icing applications where at least the minimum heat required to keep the surface water from freezing is supplied to the surface. This is because a two-dimensional phase-change model was found to be inappropriate since freezing will normally start at the liquid-air interface, which creates a problem in modeling the flow characteristics of the unfrozen water. However, since the temperature drop across the film thickness is small, the temperature may be assumed to be uniform across the layer. Therefore, when a freezing temperature, or lower, is obtained during the calculation process, an alternate method is used. This

consists of performing a macroscopic energy balance on the surface water to obtain the freezing fraction, such as done in the LEWICE code [1]. Nevertheless, the rivulet configuration and its prediction remain the same. This enables one to predict the amount and location of ice accumulation during a specified period of exposure time.

III.2 Anti-Ice Bleed Air:

The governing energy equation of the anti-ice bleed air, Eq. (12), is a first order ordinary differential equation (ODE). Due to the arbitrary distribution of the heat transfer coefficient and the wall temperature at the inside surface of the solid structure, a numerical technique must be used to solve the latter equation.

A forward finite difference scheme is only first order accurate. A more accurate and widely used technique for solving ODE's, is the fourth order Runge-Kutta method [10]. Knowing the temperature distribution in the wall, from the most recent iteration, the latter method is used to predict or update the hot air temperature distribution in the cowl. The result is subsequently used in the wall temperature solution at the next iteration.

In cases where anti-icing is achieved by means other than the hot air type (i.e., $m_a=0$), the solution of Eq. (12) using the aforementioned technique should be avoided. Instead, the air in the cowl is considered to be stagnant and at a prescribed temperature. Also, when the internal heat transfer coefficient is zero (i.e., insulated inner surfaces), there is no need to solve Eq. (12) since the result is a constant air temperature which does not affect the wall temperature, and consequently the runback water temperature.

III.3 Wall Structure:

A solution for the different layers in the wall structure may be obtained by direct approximation of the governing equation, Eq. (13), and the corresponding boundary conditions by finite differences. However, the control volume approach was chosen due to its accurate conservation properties [7]. Difference equations are derived by performing an energy balance on each control volume corresponding to a particular node. The control surfaces of each control volume are half way between the corresponding node and its adjacent surrounding nodes. There exist eleven types of nodes in the wall structure. These types are listed below and correspondingly numbered as shown in Fig 2. which illustrates a two-layer wall (note that the wall thickness dimension compared with its length is exaggerated for clarity):

1. Totally internal node.
2. Inner surface side node.
3. Inner surface left-corner node.
4. Inner surface right-corner node.
5. Left-side internal node.
6. Right-side internal node.
7. Solid-solid interface internal node.
8. Solid-solid interface left-side node.
9. Solid-solid interface right-side node.

10. Outer totally/partially wetted surface node.

11. Outer totally dry surface node.

Energy balance equations for all node types are derived and presented below. The following definitions were used:

$$\beta = \frac{\Delta z}{\Delta y}, \quad \kappa_l = \frac{k_{l+1}}{k_l}, \quad \varepsilon_l = \frac{\Delta z}{\Delta y_l}, \quad \text{and} \quad \Omega_l = \frac{\Delta y_{l+1}}{\Delta y_l} \quad (26)$$

where l and $l+1$ indicate the layer numbers corresponding to a particular solid-solid interface. Note that in the following, node (i,j) denotes the grid point at row " i " and column " j ", and that λ_i represents the distance between the two surface streamlines, defining the width of the wall strip being analyzed, at column " i ":

Node type 1:

$$\beta^2 T_{i,j-1} + \left[1 - \frac{\lambda_i - \lambda_{i-1}}{2 \lambda_i} \right] T_{i-1,j} - \left[2(\beta^2 + 1) - \frac{\lambda_i - \lambda_{i-1}}{2 \lambda_i} + \frac{\lambda_{i+1} - \lambda_i}{2 \lambda_i} \right] T_{i,j} + \left[1 + \frac{\lambda_{i+1} - \lambda_i}{2 \lambda_i} \right] T_{i+1,j} + \beta^2 T_{i,j+1} = -\frac{\Delta z^2}{k} q^\circ \quad (27)$$

Node type 2:

$$\left[2(\beta^2 + 1) - \frac{\lambda_i - \lambda_{i-1}}{2 \lambda_i} + \frac{\lambda_{i+1} - \lambda_i}{2 \lambda_i} + \frac{2 \Delta z^2 h_i}{k \Delta y} \right] T_{i,j} - \left[1 - \frac{\lambda_i - \lambda_{i-1}}{2 \lambda_i} \right] T_{i-1,j} - \left[1 + \frac{\lambda_{i+1} - \lambda_i}{2 \lambda_i} \right] T_{i+1,j} - 2 \beta^2 T_{i,j+1} = \frac{\Delta z^2}{k} \left[\frac{2}{\Delta y} (h_i T_a + q_{ai}) + q^\circ \right] \quad (28)$$

Node type 3:

If the temperature distribution is not specified at $z=0$, an insulated boundary condition is used:

$$\left[1 + \beta^2 + \frac{\lambda_{i+1} - \lambda_i}{2 \lambda_i} + \frac{\Delta z^2 h_i}{k \Delta y} \right] T_{i,j} - \left[1 + \frac{\lambda_{i+1} - \lambda_i}{2 \lambda_i} \right] T_{i+1,j} - \beta^2 T_{i,j+1} = \frac{\Delta z^2}{k} \left[\frac{1}{\Delta y} (h_i T_a + q_{ai}) + \frac{q^\circ}{2} \right] \quad (29)$$

Node type 4:

Similarly, for unspecified temperature:

$$\left[1 + \beta^2 - \frac{\lambda_i - \lambda_{i-1}}{2 \lambda_i} + \frac{\Delta z^2 h_i}{k \Delta y} \right] T_{i,j} - \left[1 - \frac{\lambda_i - \lambda_{i-1}}{2 \lambda_i} \right] T_{i-1,j} - \beta^2 T_{i,j+1} = \frac{\Delta z^2}{k} \left[\frac{1}{\Delta y} (h_i T_a + q_{ai}) + \frac{q^\circ}{2} \right] \quad (30)$$

Node type 5:

For unspecified temperature:

$$\begin{aligned}
& -\beta^2 T_{i,j-1} + \left[2(\beta^2 + 1) + \frac{\lambda_{i+1} - \lambda_i}{\lambda_i} \right] T_{i,j} \\
& - \left[2 + \frac{\lambda_{i+1} - \lambda_i}{\lambda_i} \right] T_{i+1,j} - \beta^2 T_{i,j+1} = \frac{\Delta z^2}{k} q^\circ \quad (31)
\end{aligned}$$

Node type 6:

For unspecified temperature:

$$\begin{aligned}
& -\beta^2 T_{i,j-1} - \left[2 - \frac{\lambda_i - \lambda_{i-1}}{\lambda_i} \right] T_{i-1,j} \\
& + \left[2(\beta^2 + 1) - \frac{\lambda_i - \lambda_{i-1}}{\lambda_i} \right] T_{i,j} - \beta^2 T_{i,j+1} = \frac{\Delta z^2}{k} q^\circ \quad (32)
\end{aligned}$$

Node type 7:

$$\begin{aligned}
& - \left\{ \left[\frac{1 + \kappa_l \Omega_l}{2} \right] \left[2 - \frac{\lambda_i - \lambda_{i-1}}{2\lambda_i} + \frac{\lambda_{i+1} - \lambda_i}{2\lambda_i} \right] + \varepsilon^2 \left[1 + \frac{\kappa_l}{\Omega_l} \right] \right\} T_{i,j} \\
& + \left[\frac{1 + \kappa_l \Omega_l}{2} \right] \left[1 + \frac{\lambda_{i+1} - \lambda_i}{2\lambda_i} \right] T_{i+1,j} + \varepsilon^2 \frac{\kappa_l}{\Omega_l} T_{i,j+1} = \\
& - \frac{\Delta z^2}{2k_l} [q^\circ_l + \Omega_l q^\circ_{l+1}] \quad (33)
\end{aligned}$$

Node type 8:

For unspecified temperature:

$$\begin{aligned}
& \varepsilon^2 T_{i,j-1} - \left\{ (1 + \kappa_l \Omega_l) \left[1 + \frac{\lambda_{i+1} - \lambda_i}{2\lambda_i} \right] + \varepsilon^2 \left[1 + \frac{\kappa_l}{\Omega_l} \right] \right\} T_{i,j} \\
& + (1 + \kappa_l \Omega_l) \left[1 + \frac{\lambda_{i+1} - \lambda_i}{2\lambda_i} \right] T_{i+1,j} + \varepsilon^2 \frac{\kappa_l}{\Omega_l} T_{i,j+1} = \\
& - \frac{\Delta z^2}{2k_l} [q^\circ_l + \Omega_l q^\circ_{l+1}] \quad (34)
\end{aligned}$$

Node type 9:

$$\begin{aligned}
& \varepsilon^2 T_{i,j-1} + (1 + \kappa_l \Omega_l) \left[1 - \frac{\lambda_i - \lambda_{i-1}}{2\lambda_i} \right] T_{i-1,j} \\
& - \left\{ (1 + \kappa_l \Omega_l) \left[1 - \frac{\lambda_i - \lambda_{i-1}}{2\lambda_i} \right] + \varepsilon^2 \left[1 + \frac{\kappa_l}{\Omega_l} \right] \right\} T_{i,j} \\
& + \varepsilon^2 \frac{\kappa_l}{\Omega_l} T_{i,j+1} = - \frac{\Delta z^2}{2k_l} [q^\circ_l + \Omega_l q^\circ_{l+1}] \quad (35)
\end{aligned}$$

Node type 10:

In this region, the node temperature is set equal to the local liquid temperature at the base of the film. This is achieved using a cubic spline interpolation technique because the interfacial grid points of the water and the solid do not coincide.

Node type 11:

For consistency with the lower boundary of the liquid layer, a direct differencing of the equation representing convective heat loss to the ambient is applied. This yields:

$$-T_{i,M-1} + \left(1 + \frac{h_\infty \Delta y}{k} \right) T_{i,M} = \frac{h_\infty T_\infty \Delta y}{k} \quad (36)$$

III.4 Solution Procedure:

The required solutions are the temperature distributions in the anti-ice hot air, the solid structure, and the runback water. In addition, the surface water mass flow rate and the film/rivulets configuration must be determined. A simultaneous solution must be carried in the three regions: (1) runback water; (2) solid structure; and (3) anti-ice bleed air. This may not be accomplished in a single step due to the dependency of some boundary conditions of a particular region on the final solution in the adjacent region. This suggests the use of an iterative type of numerical solution between the three regions.

The sequence of the steps utilized in the numerical solution iterative procedure may be listed as follows:

- (1) Estimate q''_m , in Eq. (18), at all nodes corresponding to the runback water at $j=1$. The procedure is to use a local one-dimensional heat transfer model from the wall to the free stream air (i.e., no conduction within the wall in the flow direction), assuming a fully dry surface. Any heat transfer generated due to electrical heating elements is assumed to flow outboard to the ambient. These assumptions were necessary to get the iterative solution started.
- (2) Compute the "initial" water temperature and the film thickness at the stagnation location from Eqs. (21) and (22), respectively.
- (3) Solve Eqs. (17), (18), and (20) for the runback water temperature distribution across the film thickness at the next z -location. Proceed with the solution of the latter equations by marching to the location of the impingement limit. This, of course, corresponds to the direct impingement region where the wetness factor is unity. Note that the runback water mass flow rate and the film thickness are updated using Eqs. (23) and (24), respectively, as the solution is brought to the next level.
- (4) From the impingement limit onward, check if the criteria for film breakup are met as the march proceeds downstream with the solution. If breakup occurs, the wetness factor and the rivulet configuration are predicted [5]. Then proceed with the calculations for each step up to the end of the structure or up to the location where total evaporation occurs. The film thickness is updated using Eq. (24) or (25), and the wetness factor is updated by geometric considerations after each Δz step.
- (5) Generally, a larger number of nodes is used in the runback water than in the wall at the solid-liquid interface. Thus, a cubic spline interpolation technique is used to predict the wall nodal temperatures, for node type 10, from the water nodal temperatures at the interface.
- (6) Setup the equations corresponding to convective boundary condition, Eq. (36), for nodes of type 11, if total evaporation occurs upstream of the end of the structure.

- (7) Assume a constant anti-ice bleed air temperature equal to the delivery temperature at the stagnation region.
- (8) Setup the equations corresponding to the rest of the solid structure nodes, types 1 through 9.
- (9) Solve the linear system of equations for the wall nodal temperatures. This terminates the first iteration.
- (10) Compute q''_m from Eq. (19) using the temperature distribution obtained in the previous step, and interpolate for the runback nodes using cubic splines. Under-relaxation of the latter values should be used to carry a stable solution as follows:

$$q''_m^{n+1} = q''_m^n + F (q''_m^{n+1} - q''_m^n)$$

where F is the under-relaxation factor and has a value between zero and unity. Its actual value depends on the particular problem under consideration.

- (11) Evidently, the solution would not converge in one iteration. Extrapolate for the initial water temperature as previously discussed, and compute the film thickness at stagnation from Eq. (22).
- (12) Repeat the runback water solution as described in steps (3) and (4).
- (13) Set the wall temperature at the solid-liquid interfacial nodes in the wet region by interpolation from the water solution of step (12). Also setup the convective boundary condition equations in the dry region as done in step (6).
- (14) Solve for the temperature of the anti-ice bleed air as described in section III.2, using the most recent wall temperature distribution at the inner surface.
- (15) Setup the equations corresponding to the remaining wall nodes as in step (8), then solve the system of linear equations for the wall nodal temperatures.
- (16) Compare the solutions obtained in the previous step with the corresponding solutions of step (5). If the difference is within an acceptable tolerance, the solution is considered converged. Otherwise, perform another iteration by repeating the last few steps starting with step (9).

IV. Sample Calculations and Discussion

The primary purpose of this paper was to present the details of the mathematical development and the numerical solution techniques of the current model. Therefore, only one example problem will be considered in order to demonstrate the calculation procedure. However, several other cases were considered and presented in Ref. [11]. The complete solution to the problem is resolved in three major steps: (1) flowfield calculations, including the viscous layer near the wall; (2) individual water droplet trajectory calculations using the velocities calculated in the previous step; and, finally, (3) the heat transfer calculations for the anti-ice hot air, the solid structure, and the surface water.

In the following example, the solid structure is assumed to be a NACA 0012 airfoil of chord length equal to 1.0 m, as illustrated in Fig. 3. The wall structure of

the airfoil is composed of five layers, typical of some aircraft surfaces. Properties and dimensions of these layers are illustrated in Table 1. The electrical heater, center layer, is assumed to be turned off and heating of the surface is accomplished by spraying hot air on the inside surface of the cowling near the stagnation region. The air is delivered at a temperature of 200 °C and a mass flow rate of 0.1 Kg/sec per unit spanwise distance.

The ambient operating conditions are the following:

- Flight Mach number = 0.25
- Ambient static temperature = -12 °C
- Ambient static pressure = 90.75 kPa
- Angle of attack = 0°
- Cloud Liquid Water Content = 1.0 g/m³
- Relative humidity = 100%
- Mean volume droplet diameter = 20 μm

The flowfield around the airfoil was computed using the ARC2D code which solves the two-dimensional thin layer Navier-Stokes equation. A hyperbolic grid generator was used to produce a C-type grid structure around the airfoil: 239 nodes along the surface and 55 nodes in the normal direction. Grids were packed near the wall for accurate prediction of the large gradients induced by viscous effects in these regions. The resulting pressure coefficient and friction coefficient distributions are illustrated in Figs. (4) and (5), respectively. These coefficients are defined as follows:

$$C_p = \frac{P - P_\infty}{\frac{1}{2} \rho_\infty V_\infty^2}$$

$$\text{and, } C_f = \frac{\tau}{\frac{1}{2} \rho_\infty V_\infty^2}$$

The first coefficient may be used to calculate properties at the edge of the boundary layer, and the second is used to compute the wall shear stress that cause the water to run back.

A particle trajectory code was then used to produce a collection efficiency distribution on the surface, as illustrated in Fig. 6. Note that all the results presented thus far are symmetric between the upper and the lower surfaces of the airfoil. This is due to the fact that the flow angle of attack is zero and the airfoil geometry is symmetric.

The final step involves the heat transfer calculations. The external convective heat transfer coefficients, between the wall surface and the ambient air, were computed using a sand roughness factor of $k_s/c=0.0002$ [1]. The internal heat transfer coefficients, between the hot air and the inner surface of the airfoil cowl were arbitrarily assumed since they depend on the particular air jet nozzles design, the rate of air flow, and the air passages geometry. These coefficients are shown in Fig. 7.

The procedure described earlier is applied, using the results thus far obtained, to solve for the problem variable parameters. The contact angle between the rivulets and the surface, when breakup of the film occurs, is assumed to be

$\beta=40^\circ$. The actual value of β depends on the properties of the solid surface and its roughness.

The resulting average temperature distribution of the anti-ice air inside the cowl is illustrated in Fig. 8. The air temperature drop across the entire length of the airfoil is approximately 85 °C. The drop occurs in a relatively smoother manner compared to that of the runback water average temperature, shown in Fig. 9. This is due to the distribution of the corresponding convective heat transfer coefficients. Since the solid wall conductivity is relatively larger than that of water, its average temperature distribution tends to be smoother as depicted in Fig. 9.

The distribution of the heat flux leaving the outer surface of the airfoil is plotted in Fig. 10. The curve peaks are due to the peaks in the distribution of the external heat transfer coefficients which correspond to a transition from laminar to turbulent flow. Figures 11 and 12 are plots of the runback water film thickness and the wetness factor, respectively. The sudden jumps in the curves correspond to the breakup of the uniform film in the direct impingement region ($F=1$) into individual rivulets ($F<1$).

The corresponding distribution of the runback surface mass flow rate per unit spanwise distance is shown in Fig. 13. This system is clearly a running wet anti-icing system. Total evaporation may be better accomplished with electrical heating elements such that a large amount of heat is supplied to the direct impingement regions.

V. Concluding Remarks

A numerical simulation for "running wet" aircraft anti-icing systems was developed. The model includes breakup of the water film, which exists in regions of direct impingement, into individual rivulets. The wetness factor distribution resulting from the film breakup and the rivulet configuration on the surface were predicted in the numerical solution. The solid wall was modeled as a multi-layer structure and the anti-icing system used was of the thermal type utilizing hot air and/or electrical heating elements embedded within the layers. The mathematical formulation of the heat transfer process as well as details of the numerical solution procedure were presented.

Experimental tests were recently conducted in the NASA Lewis Icing Research Tunnel to validate the current model. A detailed comparison with the numerical results was not possible at the time this manuscript was written since the data acquired were not reduced. However, similar trends were observed between the computer code predictions and the experimental results. Further detailed comparisons will be carried in the near future.

Acknowledgements

A portion of his work was done while the first author held a *National Research Council* Research Associateship at *NASA Lewis Research Center*. The sponsorship of these two organizations is gratefully acknowledged.

References

1. Ruff, G.A., and Berkowitz, B.M., "Users Manual for the NASA Lewis Ice Accretion Prediction Code (LEWICE)," NASA CR-185129, May 1990.
2. Cebeci, T., Chen, H.H., and Alemdaroglu, N., "Fortified LEWICE with Viscous Effects," AIAA Paper 90-0754.
3. Yamaguchi, K., Hansman, R., and Karmierczak, M., "Deterministic Multi-Zone Ice Accretion Modeling," AIAA Paper 91-0265.
4. Hansman, R.J., Yamaguchi, K., Berkowitz, B., and M. Potapczuk, "Modeling of Surface Roughness Effects on Glaze Ice Accretion," AIAA Paper 89-0734, Jan 1989.
5. Al-Khalil, K.M., Keith, T.G., De Witt, K.J., "Development of an Anti-Icing Runback Model," AIAA Paper 90-0759, Jan 1990.
6. Al-Khalil, K.M., Keith, T.G., De Witt, K.J., "Further Development of an Anti-Icing Runback Model," AIAA Paper 91-0266, Jan 1991.
7. Al-Khalil, K.M., "Numerical Simulation of an Aircraft Anti-Icing System Incorporating a Rivulet Model for the Runback Water," PhD Dissertation, University of Toledo, Toledo, Ohio, June 1991.
8. Gelder, T. F., and Lewis, J. P., "Comparison of Heat Transfer from Airfoil in Natural and Simulated Icing Condition," NACA TN - 2480, September, 1951.
9. Anderson, D.A., Tannehill, J.C., and Pletcher, R.H., *Computational Fluid Mechanics and Heat Transfer*, Hemisphere Pub. Corp., 1984.
10. Carnahan, B., Luther, H. A., and Wilkes, J. O., *Applied Numerical Methods*, John Wiley & Sons, Inc., 1969, pp. 363-366.
11. Al-Khalil, K.M., Keith, T.G., De Witt, K.J., "Development of an Improved Model for the Runback Water on Aircraft Surfaces," AIAA Paper 92-0042, Jan 1992.

Table 1: Composite Wall Physical and Thermal Properties.

Layer number	Description	Material	Thickness (mm)	Thermal Conductivity (W/m.K)
1	Substrate	Aluminum Alloy	2.20	220
2	Inner Insulation	Epoxy/Glass	1.30	1.25
3	Heater*	Copper	0.20	340
4	Outer Insulation	Epoxy/Glass	0.25	1.25
5	Abrasion Shield	Stainless Steel	0.30	50

*Heater turned off

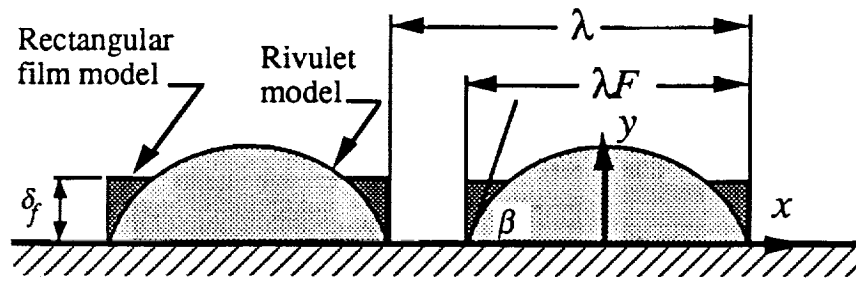


Fig. 1: Rivulet and equivalent rectangular film models.

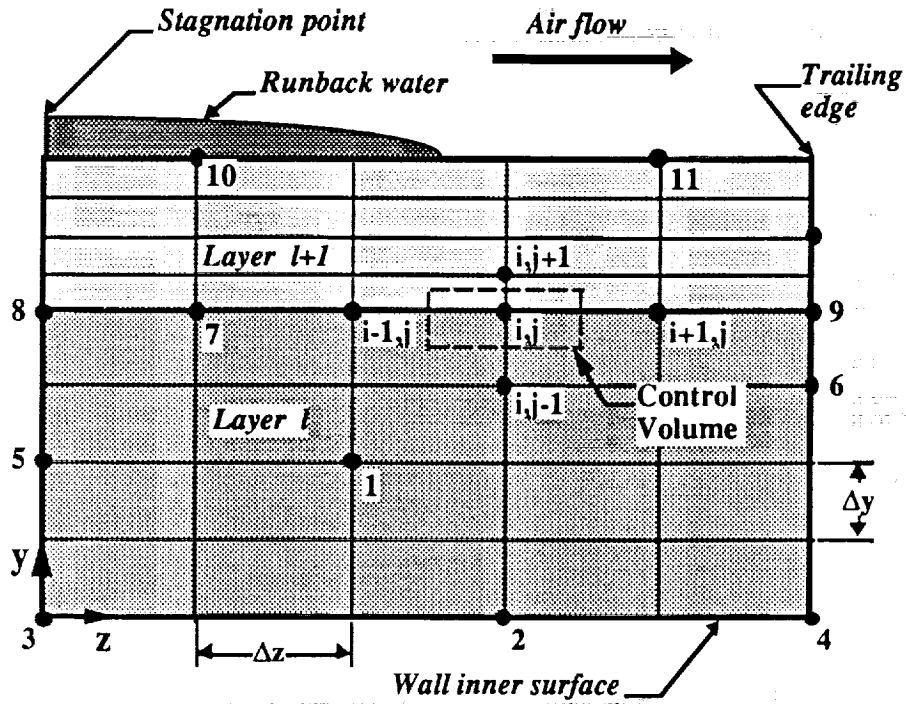


Fig. 2: Type of grid points in the wall.

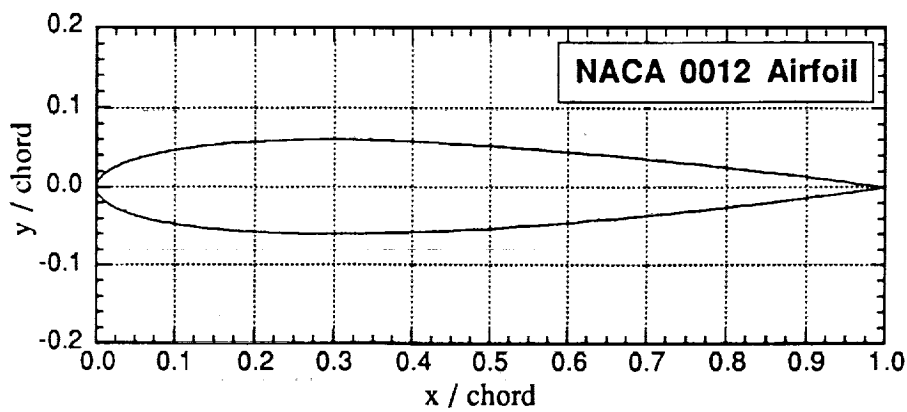


Fig. 3: NACA 0012 airfoil geometry.

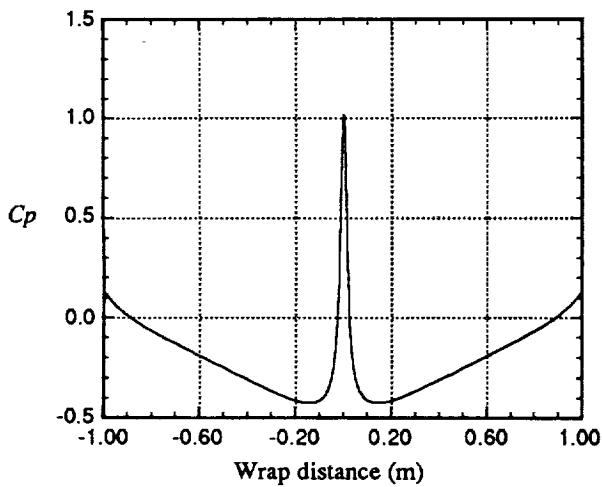


Fig. 4: Surface pressure coefficient.

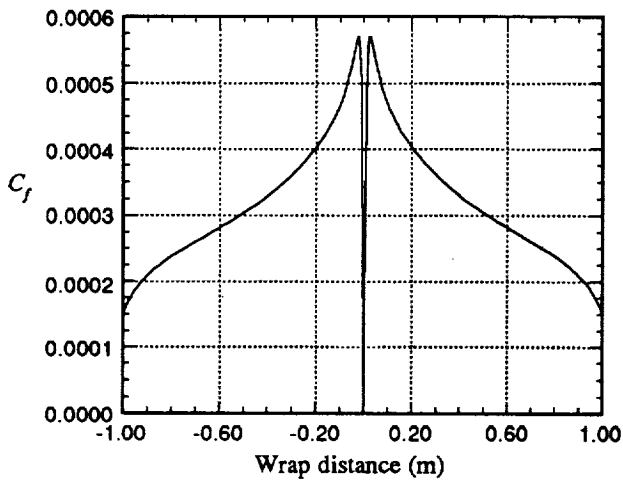


Fig. 5: Skin friction coefficient.

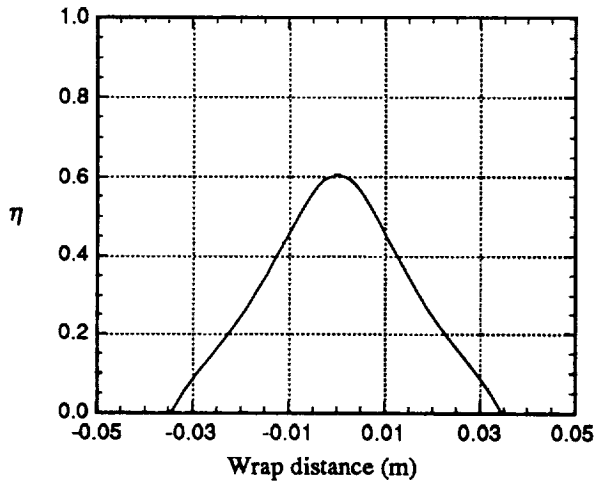


Fig. 6: Droplet collection efficiency.

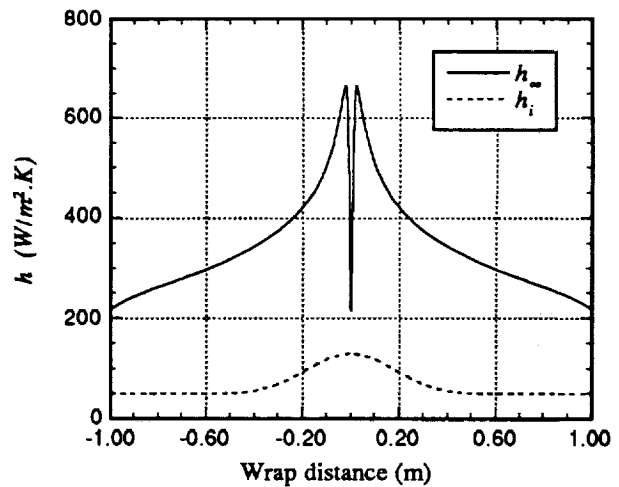


Fig. 7: Internal and external heat transfer coefficients.

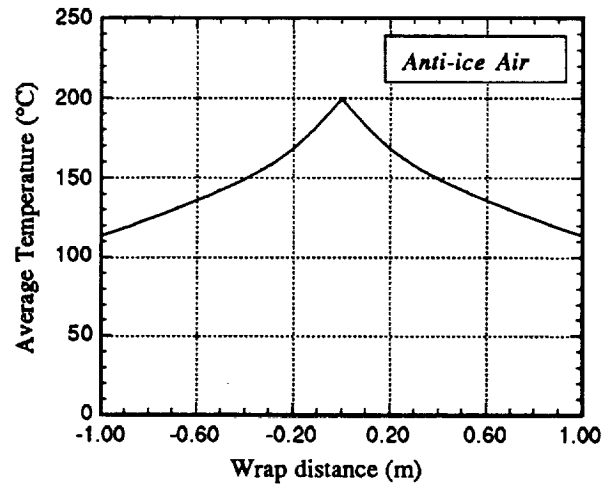


Fig. 8: Anti-ice air temperature.

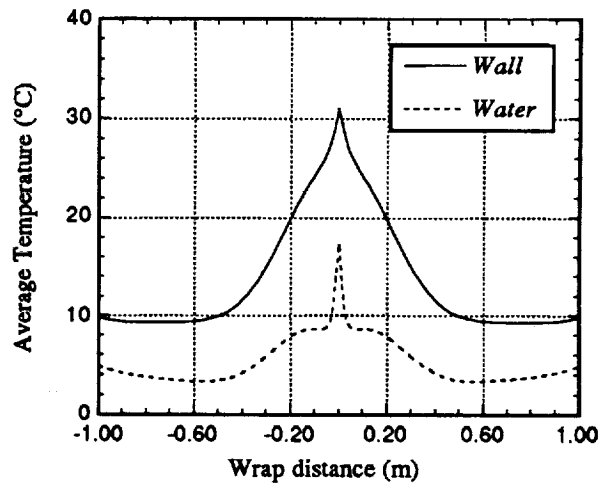


Fig. 9: Average water and wall temperatures.

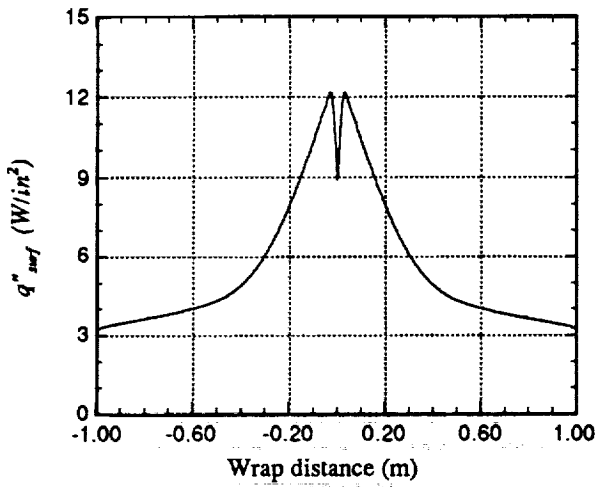


Fig. 10: Surface heat flux.

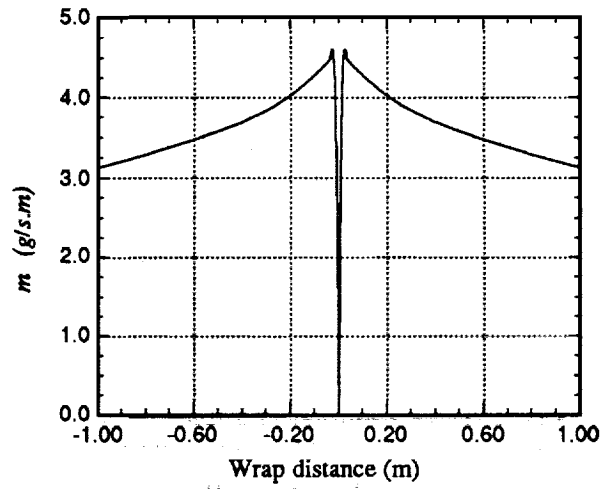


Fig. 13: Surface water mass flow rate.

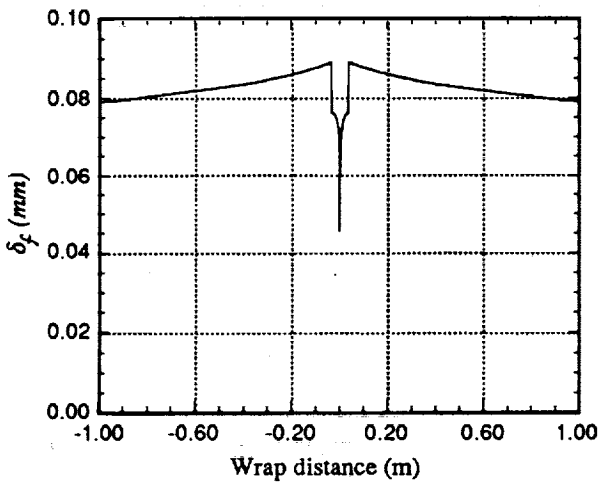


Fig. 11: Runback water film thickness.

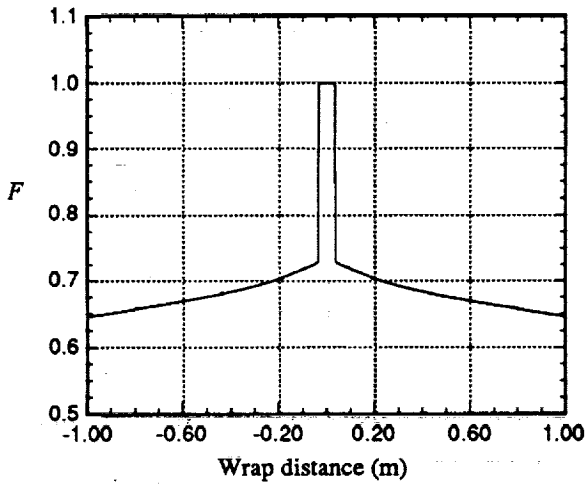


Fig. 12: Wetness factor.